Batteries Hot Paper

International Edition: DOI: 10.1002/anie.201912634
German Edition: DOI: 10.1002/ange.201912634

Proton Intercalation/De-Intercalation Dynamics in Vanadium Oxides for Aqueous Aluminum Electrochemical Cells

Qing Zhao, Luojia Liu, Jiefu Yin, Jingxu Zheng, Duhan Zhang, Jun Chen, and Lynden A. Archer*

Abstract: *Understanding cation (H^+, Li^+, Na^+, Al^{3+}, etc.) intercalation/de-intercalation chemistry in transition metal compounds is crucial for the design of cathode materials in aqueous electrochemical cells. Here we report that orthorhombic vanadium oxides (V_2O_5) supports highly reversible proton intercalation/de-intercalation reactions in aqueous media, enabling aluminum electrochemical cells with extended cycle life. Empirical analyses using vibrational and x-ray spectroscopy are complemented with theoretical analysis of the electrostatic potential to establish how and why protons intercalate in V_2O_5 in aqueous media. We show further that cathode coatings composed of cation selective membranes provide a straightforward method for enhancing cathode reversibility by preventing anion cross-over in aqueous electrolytes. Our work sheds light on the design of cation transport requirements for high-energy reversible cathodes in aqueous electrochemical cells.*

The chemistry of Li^+ in solid-state electrode materials has played a critical role in enabling the current commercial dominance of rechargeable Li-ion battery technology.[1] The electrochemical instability of water at the potentials of interest in a Li-ion battery has nonetheless limited application of this knowledge to aprotic electrolytes, where competition from other mobile ions such as H^+ and hydroxyl (OH^-) is avoided.[2] With increasing interest in electrochemical storage technologies that provide intrinsically safe and lower cost options to Li-ion batteries, electrode chemistries that are able to selectively and reversibly intercalate cations in aqueous media are drawing increasing interest. There is likewise a growing number of reports detailing promising energy storage/conversion systems in various form factors, for example, redox flow batteries,[3] zinc/Al batteries,[2b,4] Li/Na/K-ion batteries,[2a,5] that must be operated reversibly in aqueous electrolyte media.

Aqueous electrochemical cells based on Al are of particular interest here because of their significant potential for improving safety, cost, and manufacturability gains, relative to other secondary battery chemistries.[6] The Al anode also provides up to three charge equivalents per mole, endowing it with among the highest storage capacities by volume ($8040\ \mathrm{mAh\,cm^{-3}}$).[6,7] Very recently,[4c] it was shown that one of the key barriers to achieving high levels of reversibility of an Al anode in aqueous electrolyte media, namely the propensity of the metal to react with water to form a high band-gap passivating Al_2O_3 oxide layer, is removed by protecting Al with an artificial, solid-state electrolyte interphase formed by pretreatment with an ionic liquid electrolyte. Here we consider the enormous challenge of designing a cathode capable of supporting reversible intercalation/de-intercalation reactions in an aqueous electrolyte. To begin, we note that while the radius of Al^{3+} (53.5 pm) is smaller than Li^+ (76 pm), the high charge density of Al^{3+} ($748\ \mathrm{C/mm^3}$) versus Li^+ ($87\ \mathrm{C/mm^3}$) simultaneously increases the difficulty of de-solvating the Al^{3+} cation at the cathode and presents a formidable challenge in finding stable solid-state cathode hosts that remain intact under the large periodic stresses induced by the large electrostatic forces created by intercalation and de-intercalation of Al^{3+}.[6b] These challenges are compounded in acidic aqueous electrolyte media containing dissociable Al salts, which may contain comparable concentrations of smaller and more mobile H^+ ions that can compete with Al^{3+} for intercalation sites in the cathode. V_2O_5 has been reported in the earliest Al-ion battery chemistries, which utilized ionic liquid electrolytes.[7e] Subsequent high-resolution TEM and spectroscopic studies indicate that while Al^{3+} can reversibly insert into V_2O_5, the kinetics are sluggish.[8]

In this communication, we report on the effect of electrolyte composition and pH on the selectivity and reversibility of H^+ and other cations in V_2O_5 cathodes in aqueous aluminum electrochemical cells. We compare our findings with theoretical calculations, which show that the insertion of at least one proton in the V_2O_5 structure is always favored in acidic electrolyte media and that V_2O_5 undergoes at most a 12.3% volume change. We report further that selectivity of V_2O_5 for various cations in more basic electrolytes is largely regulated by the relative ion concentration and charge density. Finally,

---

[*] Q. Zhao, J. Yin, Prof. L. A. Archer
Robert Frederick Smith School of Chemical and Biomolecular Engineering, Cornell University
Ithaca, NY 14853 (USA)
E-mail: laa25@cornell.edu

L. Liu, Prof. J. Chen
State Key Laboratory of Elemento-Organic Chemistry and Key Laboratory of Advanced Energy Materials Chemistry (Ministry of Education), College of Chemistry, Nankai University
Tianjin 300071 (China)

J. Zheng, Prof. L. A. Archer
Department of Materials Science and Engineering
Cornell University
Ithaca, NY (USA)

D. Zhang
Department of Mechanical and Aerospace Engineering
Cornell University
Ithaca, NY 14853 (USA)

Supporting information and the ORCID identification number(s) for the author(s) of this article can be found under: https://doi.org/10.1002/anie.201912634.

© 2019 Wiley-VCH Verlag GmbH & Co. KGaA, Weinheim

we show that an interlayer membrane that facilitates selective cation transport into the V_2O_5 cathode promotes reversibility of the cathode by simultaneously enabling cation de-solvation[9] and by preventing anion insertion into V_2O_5.

V_2O_5 with a nanorod morphology was synthesized using a hydrothermal method (Figure 1 a,b, Figure S1).[7b] The resultant orthorhombic V_2O_5 shows a typical layered structure, in which the (001) crystal planes (located at 20.4°) are spaced approximately 4.37 Å apart. Galvanostatic analysis of the V_2O_5 cathode in an aqueous Al || V_2O_5 cell containing 2 m $Al(OTf)_3$ (electrolyte pH ≈ 2) shows a single discharge plateau at approximately 0.9 V, and a corresponding charge plateau at approximately 1.1 V (Figure 1 c). The discharge capacity for the first cycle is 186 $mAh\,g^{-1}$, which corresponds to a little more than one electron reaction per V_2O_5 molecule. In the following cycles, the discharge capacity and Coulombic Efficiency (CE) decays quickly, but the discharge/charge plateaus remain unchanged, indicating that the electrode reactions are reversible. We will show later that the fast fall-off in capacity and Coulombic efficiency are the result of dissolution of the V_2O_5 electrode in the acidic electrolyte medium.

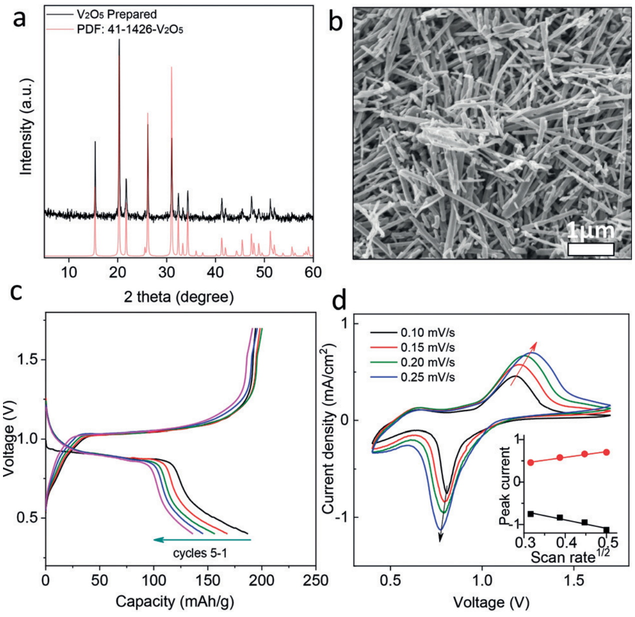

Figure 1. Electrochemical performance of aqueous aluminum || V_2O_5 cells. a) Measured and tabulated XRD profiles for V_2O_5. b) SEM image of the prepared V_2O_5. c) Galvanostatic discharge/charge curves for aqueous Al || V_2O_5 cells at a current density of 40 $mA\,g^{-1}$. d) Cyclic voltammograms measured at 0.10. 0.15, 0.20, and 0.25 $mV\,s^{-1}$. The inset shows that the cathodic and anodic peak currents are proportional to the square root of scan rate.

SEM (Supporting Information, Figure S2) accompanied with EDX analysis (Table S1) indicate that the oxidized aluminum mainly forms a soluble product on the surface of V_2O_5 after discharge, rather than intercalating into the V_2O_5 layer (Detailed analysis provided in the Supporting Information). CV measurements at different scan rates are used to understand the charge transport processes in the V_2O_5 cathode (Figure 1 d). One major reduction peak and one oxidation peak can be observed at different scan rates. Due to the enhanced polarization after increasing scan rate, the reduction peaks are shifted to lower potentials and the oxidation peaks shifted to higher potentials at high scan rate. The peak current density of both peaks is proportional to the square root of the scan rate (inset to Figure 1 d), indicating that diffusion-limited Faradaic reactions occur at the V_2O_5 electrode. The associated diffusion coefficients were estimated using the Randles–Sevcik equation and found to be approximately 1.3×10^{-10} $cm^2\,s^{-1}$, for intercalation, and 0.6×10^{-10} $cm^2\,s^{-1}$ for the de-intercalation reaction.

It is reasonable to hypothesize that at the low electrolyte pH used in the experiments, H^+ preferentially intercalates into the V_2O_5 electrode, relative to Al^{3+}. We evaluated this hypothesis by interrogating V_2O_5 electrodes at different states of discharge/charge. Insets in Figure 2 a show that the electrode undergoes a noticeable change in color at each time increment. Whereas, the pristine V_2O_5 cathode is yellow in color, which is the typical color of V^{5+} compounds, after discharge the electrode gradually turns darker, indicative of the reduction of V_2O_5. This process is reversible, and the color of the electrode returns to yellow after fully charging the Al || V_2O_5 cell, confirming that reversible redox vanadium chemistry is the source of the voltage plateaus measured in the galvanostatic charging and discharging experiments. XRD analysis was used to study changes in structure of V_2O_5 electrodes at different stages of charge and discharge (Figure 2 b). The XRD patterns are largely stable after discharge, indicating that the crystal structure of V_2O_5 remains intact. One significant change, however, is the shift of the (001) crystal lattice after full discharge (2θ changes from 20.4° to 21.3°), indicating that the V_2O_5 layers shrink from approximately 4.4 Å to 3.83 Å, as estimated using the Bragg equation ($n\lambda = 2d\sin\theta$). The fully discharged XRD patterns can be well fitted to the reported pattern for $H_{1.43}V_2O_5$. We will show later that this change is consistent with expectations from theoretical analysis.

Our assertion that the Faradaic reactions in the Al || V_2O_5 aqueous cell are the result of proton intercalation in V_2O_5 is supported by the FTIR analysis in Figure 2 c. For pristine V_2O_5, the IR peaks located at 1018 cm^{-1} and 617 cm^{-1} may be assigned to vibrations associated with V=O and V−O−V bonds, respectively. The peak at about 829 cm^{-1} is assigned to the coupled vibrations of V=O and V−O−V bond.[10] After discharge, the V=O peak is observed to shift to lower wavenumber, indicating the weakening of the V=O bond; the peak associated with the V−O−V bond shifts to higher value, indicating the increased strength of this bond. In addition to the intensity change, new peaks located at 3504 cm^{-1} emerge after full discharge, and are assigned to the -OH bend. We note further that these peaks are quite different from the distinctive broad -OH bend (broad peak at 3347 cm^{-1}) associated with liquid water. Our observations are consistent with the hypothesis that upon full cell discharge, protons insert into the cathode, forming coordinated O−H bonds in V_2O_5 structures.[10b]

More detailed information of the structure evolution of V_2O_5 can be obtained from Raman scattering studies of the

© 2019 Wiley-VCH Verlag GmbH & Co. KGaA, Weinheim

15213773, 2020, 8, Downloaded from https://onlinelibrary.wiley.com/doi/10.1002/anie.201912634 by Massachusetts Institute of Technolo, Wiley Online Library on [08/08/2023]. See the Terms and Conditions (https://onlinelibrary.wiley.com/terms-and-conditions) on Wiley Online Library for rules of use; OA articles are governed by the applicable Creative Commons License

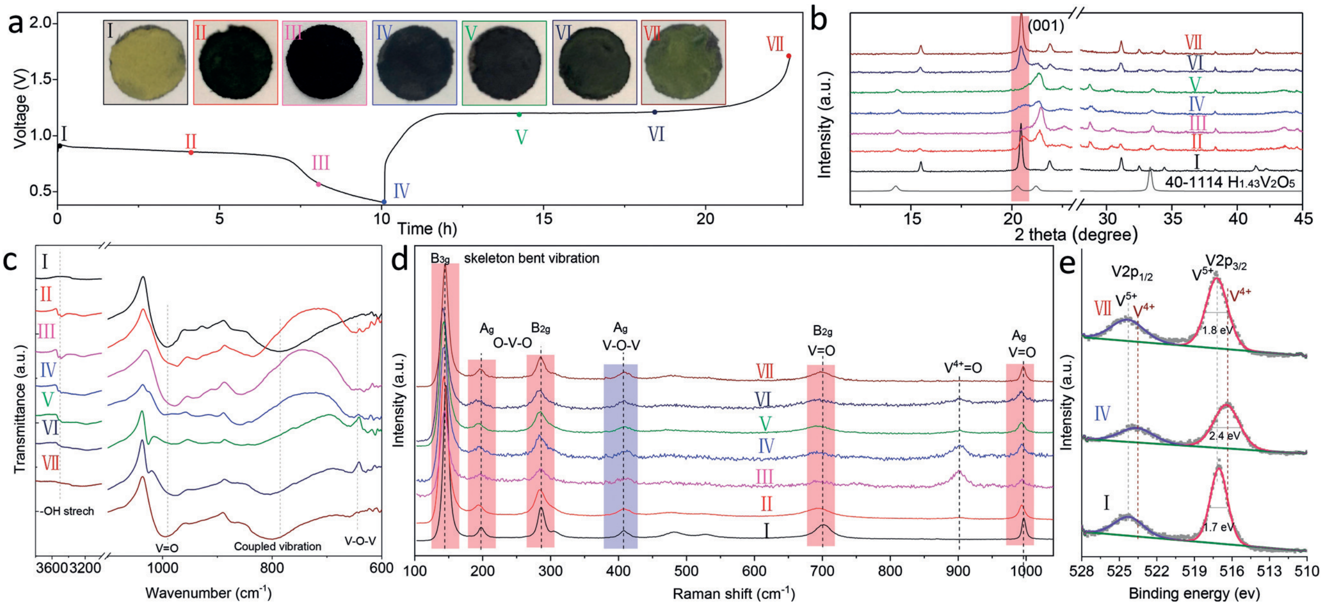

Figure 2. Proton intercalation/de-intercalation of V_2O_5 electrode in aqueous electrochemical cells. a) Galvanostatic discharge/charge curves of aqueous Al electrochemical cells using V_2O_5 cathodes at current density of 20 mA g^{-1}, in which different discharge/change states marked as I, II, III, IV, V, VI, VII (as shown in digital photos) are selected for characterizations. Corresponding characterizations of marked points using b) XRD patterns, c) FTIR spectra, d) Raman spectra, e) XPS spectra.

electrode (Figure 2d). An obvious change apparent in the Raman spectra is the red shift of the A_g symmetric vibration, which is related to the shortest vanadium–oxygen bond (vanadyl V=O), shifting from 997 cm^{-1} to 993 cm^{-1} after full cell discharge. Meanwhile, the B_{2g} vibration associated with the V=O bond also shifts from 700 cm^{-1} to 693 cm^{-1} after discharge.[11] Both observations can be explained in terms of changes in bonding induced by insertion of H^+ in the V_2O_5 layers. The elongation of the vanadyl bond is consistent with lowering of the bond energy and explains the red shift of the V=O vibration. The red shifts observed for the vibrations located at 198 cm^{-1} (A_g) and 286 cm^{-1} (B_{2g}) can also be explained in similar terms. Assigned to the δ(O−V−O) distortion modes, which also include a short vanadium-oxygen double bond, the red-shift of these bonds indicate that the skeleton of V_2O_5 becomes weaker as might be expected after H-insertion (B_{3g}). The corresponding blue shift (from 407 cm^{-1} to 411 cm^{-1}) of the Ag mode (δ(V−O−V)) after full discharge, can be interpreted as a strengthening of the V−O−V bond after wakening of the vanadyl. Finally, the new peak located at approximately 900 cm^{-1} after discharge, is assigned to the V^{4+}=O vibration,[11c] consistent with expectations for H insertion. Further support for H insertion was obtained from electrochemical studies in which the weak acid CH_3COOH (HAC) was used as electrolyte. Al || V_2O_5 cells based on this electrolyte deliver similar discharge capacity as those in which $Al(OTf)_3$ is used as electrolyte (Figure S3a). FTIR (Figure S3b) and XRD (Figure S3c) spectra of the V_2O_5 cathode after full cell discharge reveal no noticeable differences for the HAC or $Al(OTf)_3$ electrolytes. Although the concentration of protons is low according ($\approx$10 mM) in the latter electrolyte, the solvated Al^{3+} cation, $[Al(H_2O)_6]^{3+}$, can be considered as an abundant latent source of protons.[12]

XPS analysis was performed to directly determine the valence change of V_2O_5 after the discharge/charge reactions (Figure 2e). The pristine V_2O_5 is seen to exhibit typical V^{5+}, in which the sharp $V_{2p3/2}$ peak located at 517.1 eV is accompanied by a $V_{2p1/2}$ peak located at 524.3 eV.[13] Both peaks shift to lower energy and become broader after full discharge. The $V_{2p3/2}$ peak located at 516.3 eV, $V_{2p1/2}$ peak located at 523.5 eV, indicating the mixed valence of vanadium (mostly V^{4+}). The full width at half maximum (FWHM) for both peaks is also observed to largely increase after discharge, confirming the reduction of V_2O_5.

In order to determine the cause of the capacity fading in aqueous Al || V_2O_5 batteries, we performed postmortem analysis of the battery components after cycling. The analysis shows that the glass fiber separator turns yellow after cycling, suggesting that exfoliation and dissolution of the active material is the source of the capacity fading, and possibly also of the low coulombic efficiency (Figures S4 and S5). The dissolution of vanadium oxides in aqueous media is well known to involve $HV_2O_5^-$, $H_3V_2O_7^-$, or VO_2^+ species, depending on electrolyte pH and the valence of vanadium.[14] The dissolved anion spices are able to diffuse in the interelectrode space and to be reduced on the anode side. A Nafion™ coated 3501 membrane was used as a protection layer on V_2O_5 cathode (Figure S6) to limit the free cross-over of the anion. Figure 3a shows the discharge/charge profiles for the first thirty cycles in cells with the protective layer. The profiles are qualitatively similar to those obtained without the Nafion layer. However, the columbic efficiency and cycling stability is much improved. A capacity of 120 mAh g^{-1} is retained after 50 cycles (Figure 3b), which compares favorably to the capacity of 20 mAh g^{-1} remaining after 50 charge/discharge cycles for cells without nafion protection (control

© 2019 Wiley-VCH Verlag GmbH & Co. KGaA, Weinheim

15213773, 2020, 8, Downloaded from https://onlinelibrary.wiley.com/doi/10.1002/anie.201912634 by Massachusetts Institute of Technolo, Wiley Online Library on [08/08/2023]. See the Terms and Conditions (https://onlinelibrary.wiley.com/terms-and-conditions) on Wiley Online Library for rules of use; OA articles are governed by the applicable Creative Commons License

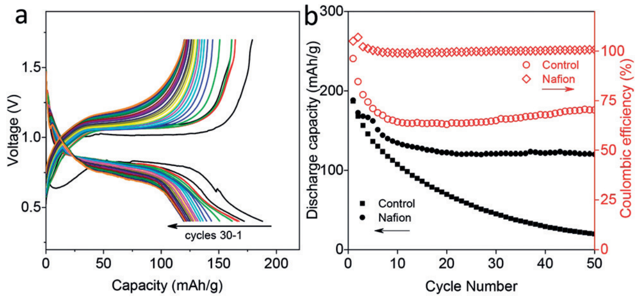

Figure 3. Proton intercalation/de-intercalation characteristics of V_2O_5 protected by a cation-selective membrane. a) Galvanostatic discharge/charge profiles of aqueous Al/V_2O_5 batteries using Nafion modified separator. b) Corresponding cycling performance and coulombic efficiency.

profiles). The digital pictures shown in Figure S3a also support our hypothesis. The glass fiber separator is observed to retain its white coloration after cycling studies in cells that utilize the Nafion membrane. The increased polarization apparent from the results is attributed to the Al anode (Figure S7).

A more precise understanding of the proton insertion reaction in V_2O_5 is possible from numerical simulations. The Electrostatic potential (ESP) of a V_2O_5 cluster is firstly calculated to obtain the possible reaction sites, then the crystal structure is optimized by density functional theory (DFT) to obtain the crystal structure of V_2O_5 after one or two proton insertions.[15] Figure 4a shows that the pristine V_2O_5 exhibits a typical layered structure. The distance between two vanadium atoms is 4.37 Å, corresponding to the (001) crystal plane of V_2O_5. The distance between the vanadium and oxygen atoms is 1.58 Å, which is the shortest distance between vanadium and oxygen (V=O). Figure 4b shows the crystal structure of V_2O_5 after insertion of one proton (HV_2O_5), which would produce a specific capacity of 147 $mAh\,g^{-1}$ in a V_2O_5 cathode—close to the capacity delivered in the Al || V_2O_5 cells. Although the results show that HV_2O_5 is strictly triclinic, the crystal structure is very close to orthorhombic ($\alpha = 89.39°$, $\beta = 89.98°$, $\gamma = 89.90°$). The c-axis obviously shrinks after proton insertion and the interlayer distance reduces from 4.37 Å to 3.86 Å, which is well in accordance with the right shift of (001) peak apparent in the XRD (Figure 2b), and the V=O bond length becomes longer (from 1.58 Å to 1.60 Å). The volume reduction can be calculated to be 12.3%. The analysis also reveals an O−H bond length of 0.99 Å, which is different from its typical value of 0.96 Å in a water molecule, explaining the FTIR spectra. We also simulated the corresponding changes in crystal structure of V_2O_5 that would occur if two protons are intercalated (Figure S8), which would produce a specific capacity of 296 $mAh\,g^{-1}$ in a V_2O_5 cathode. $H_2V_2O_5$ exhibits a triclinic structure ($\alpha = 115.48°$, $\beta = 90.01°$, $\gamma = 90.00°$) with much shorted layer distance (3.54 Å) and a volume reduction of 37.5%. The large volume change after the two-proton insertion indicates that despite the higher specific capacity, the two-proton insertion would likely destabilize the structure of the V_2O_5 cathode not stable for battery performance.

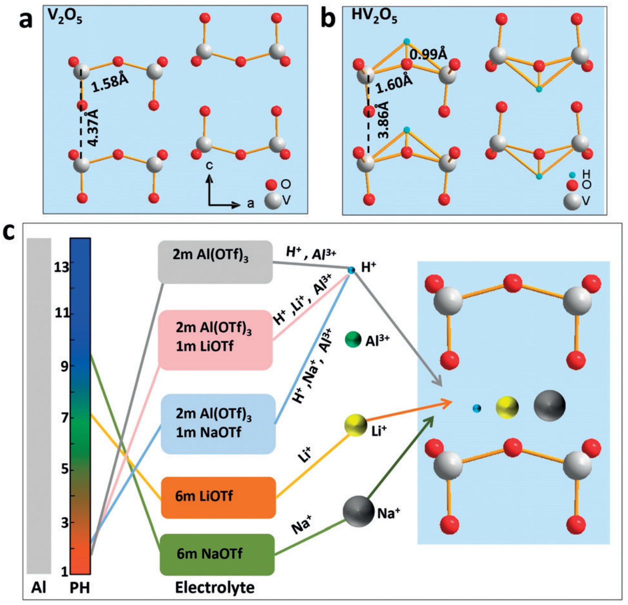

Figure 4. Cation intercalation/de-intercalation principles of V_2O_5 in aqueous aluminum cells. Structure of a) pristine V_2O_5 and b) after proton insertion. c) Different cation intercalating behaviors of V_2O_5 through regulating the electrolytes.

In order to assess the stability of the proton insertion chemistry in V_2O_5 cathodes, we studied the effect of competing mobile cations on the composition of the discharged cathode. The results show that the cation intercalation of V_2O_5 is controlled by both pH and ion concentration. In an acid environment, H^+ is the dominant cation inserted into V_2O_5, even in the presence of other mobile metal ions. For example, in electrolytes composed of 2 m $Al(OTf)_3$ + 1 m Li(OTf) (pH ≈ 2) or 2 m $Al(OTf)_3$ + 1 m Na(OTf) (pH ≈ 2–3), the galvanostatic discharge/charge profiles are similar to those found in the pure $Al(OTf)_3$ electrolytes (Figure S9). No other metal ions are detected in the structure of V_2O_5 (Figure S10). In contrast, in more basic electrolytes, (e.g. 6 m LiOTf (pH ≈ 7–8) or 6 m NaOTf (pH ≈ 9–10)), the galvanostatic discharge/charge profiles are noticeably different from those containing $Al(OTf)_3$ (Figure S11). Results from XRD and FTIR analyses of the cathode after discharge are indicative of $Li_{1.03}V_2O_5$ for pure LiOTf based electrolytes (Figure S12). The EDX spectra also clearly demonstrate participation of sodium after discharge in pure NaOTf based electrolytes. The expected product is $Na_{0.6\pm0.1}V_2O_5$ (Figure S13). When tuning the pH values of LiOTf (6 m) and NaOTf (6 m) electrolytes to around 2–3 with the addition of HAC, the major insertion cation for NaOTf electrolyte becomes a proton while for LiOTf it is still Li^+ (Figure S14). However, in no case, we have found the interaction of Al^{3+} in V_2O_5 in aqueous electrochemical cells, which may be due to high charge density of the multivalent Al^{3+} of Al-ion. The high charge density of Al-ion increases the difficulty of dissociation and results in the bigger active cation in practical situation (for example, $Al(OTf)_2^{+}$, or $Al(OTF)^{2+}$).

In conclusion, we discover the reversible proton intercalation/de-intercalation chemistry in aqueous aluminum electrochemical cells. The proton reaction in acid electrolyte

15213773, 2020, 8, Downloaded from https://onlinelibrary.wiley.com/doi/10.1002/anie.201912634 by Massachusetts Institute of Technolo, Wiley Online Library on [08/08/2023]. See the Terms and Conditions (https://onlinelibrary.wiley.com/terms-and-conditions) on Wiley Online Library for rules of use; OA articles are governed by the applicable Creative Commons License

15213773, 2020, 8, Downloaded from https://onlinelibrary.wiley.com/doi/10.1002/anie.201912634 by Massachusetts Institute of Technolo, Wiley Online Library on [08/08/2023]. See the Terms and Conditions (https://onlinelibrary.wiley.com/terms-and-conditions) on Wiley Online Library for rules of use; OA articles are governed by the applicable Creative Commons License

provides a capacity of $\approx 200\,\mathrm{mAh\,g^{-1}}$ with high reversibility over 50 cycles. Further studies reveal that the cation (H^+, Li^+, Na^+, Al^{3+}, et al.) intercalation/de-intercalation chemistry can be rationally designed by regulating by ion concentration (PH) and components in the electrolytes. Our work provides a new pathway to design host materials for aqueous electrochemical cells.

Acknowledgements

This work was supported by the Department of Energy Basic Energy Sciences Program through Award#: DE-SC0016082. Electron microscopy facilities at the Cornell Center for Materials Research (CCMR), an NSF-supported MRSEC through grant DMR-1719875, were also used for the study.

Conflict of interest

The authors declare no conflict of interest.

Keywords: Al battery · aqueous battery · cathode materials · cation selection · nanorods

How to cite: *Angew. Chem. Int. Ed.* **2020**, *59*, 3048–3052
Angew. Chem. **2020**, *132*, 3072–3076

---

[1] a) M. Armand, J. M. Tarascon, *Nature* **2008**, *451*, 652–657; b) B. Dunn, H. Kamath, J. M. Tarascon, *Science* **2011**, *334*, 928–935; c) J. B. Goodenough, K. S. Park, *J. Am. Chem. Soc.* **2013**, *135*, 1167–1176; d) M. S. Whittingham, *Chem. Rev.* **2004**, *104*, 4271–4302.

[2] a) H. Kim, J. Hong, K. Y. Park, S. W. Kim, K. Kang, *Chem. Rev.* **2014**, *114*, 11788–11827; b) W. Sun, F. Wang, S. Hou, C. Yang, X. Fan, Z. Ma, T. Gao, F. Han, R. Hu, M. Zhu, C. Wang, *J. Am. Chem. Soc.* **2017**, *139*, 9775–9778; c) X. Wang, C. Bommier, Z. Jian, Z. Li, R. S. Chandrabose, I. A. Rodriguez-Perez, P. A. Greaney, X. Ji, *Angew. Chem. Int. Ed.* **2017**, *56*, 2909–2913; *Angew. Chem.* **2017**, *129*, 2955–2959; d) R. Emanuelsson, M. Sterby, M. Stromme, M. Sjodin, *J. Am. Chem. Soc.* **2017**, *139*, 4828–4834.

[3] G. L. Soloveichik, *Chem. Rev.* **2015**, *115*, 11533–11558.

[4] a) D. Kundu, B. D. Adams, V. Duffort, S. H. Vajargah, L. F. Nazar, *Nat. Energy* **2016**, *1*, 16119; b) Q. Zhao, W. Huang, Z. Luo, L. Liu, Y. Lu, Y. Li, L. Li, J. Hu, H. Ma, J. Chen, *Sci. Adv.* **2018**, *4*, eaao1761; c) Q. Zhao, M. J. Zachman, W. I. Al Sadat, J. Zheng, L. F. Kourkoutis, L. Archer, *Sci. Adv.* **2018**, *4*, eaau8131; d) G. G. Yadav, J. W. Gallaway, D. E. Turney, M. Nyce, J. Huang, X. Wei, S. Banerjee, *Nat. Commun.* **2017**, *8*, 14424; e) J. Zheng, Q. Zhao, T. Tang, J. Yin, C. D. Quilty, G. D. Renderos, X. Liu, Y. Deng, L. Wang, D. C. Bock, C. Jaye, D. Zhang, E. S. Takeuchi, K. J. Takeuchi, A. C. Marschilok, L. A. Archer, *Science* **2019**, *366*, 645–648; f) F. Wan, Z. Niu, *Angew. Chem. Int. Ed.* **2019**, *58*, 16358–16367; *Angew. Chem.* **2019**, *131*, 16508–16517.

[5] a) H. Gao, J. B. Goodenough, *Angew. Chem. Int. Ed.* **2016**, *55*, 12768–12772; *Angew. Chem.* **2016**, *128*, 12960–12964; b) C. Liu, X. Wang, W. Deng, C. Li, J. Chen, M. Xue, R. Li, F. Pan, *Angew. Chem. Int. Ed.* **2018**, *57*, 7046–7050; *Angew. Chem.* **2018**, *130*, 7164–7168; c) Q. Zheng, S. Miura, K. Miyazaki, S. Ko, E. Watanabe, M. Okoshi, C. P. Chou, Y. Nishimura, H. Nakai, T. Kamiya, T. Honda, J. Akikusa, Y. Yamada, A. Yamada, *Angew. Chem. Int. Ed.* **2019**, *58*, 14202–14207; *Angew. Chem.* **2019**, *131*, 14340–14345; d) L. W. Jiang, Y. X. Lu, C. L. Zhao, L. L. Liu, J. N. Zhang, Q. Q. Zhang, X. Shen, J. M. Zhao, X. Q. Yu, H. Li, X. J. Huang, L. Q. Chen, Y. S. Hu, *Nat. Energy* **2019**, *4*, 495–503.

[6] a) G. A. Elia, K. Marquardt, K. Hoeppner, S. Fantini, R. Lin, E. Knipping, W. Peters, J. F. Drillet, S. Passerini, R. Hahn, *Adv. Mater.* **2016**, *28*, 7564–7579; b) J. Muldoon, C. B. Bucur, T. Gregory, *Chem. Rev.* **2014**, *114*, 11683–11720.

[7] a) T. Gao, X. Li, X. Wang, J. Hu, F. Han, X. Fan, L. Suo, A. J. Pearse, S. B. Lee, G. W. Rubloff, K. J. Gaskell, M. Noked, C. Wang, *Angew. Chem. Int. Ed.* **2016**, *55*, 9898–9901; *Angew. Chem.* **2016**, *128*, 10052–10055; b) N. Jayaprakash, S. K. Das, L. A. Archer, *Chem. Commun.* **2011**, *47*, 12610–12612; c) M. C. Lin, M. Gong, B. Lu, Y. Wu, D. Y. Wang, M. Guan, M. Angell, C. Chen, J. Yang, B. J. Hwang, H. Dai, *Nature* **2015**, *520*, 325–328; d) Y. Hu, B. Luo, D. Ye, X. Zhu, M. Lyu, L. Wang, *Adv. Mater.* **2017**, *29*, 1606132; e) D. J. Kim, D.-J. Yoo, M. T. Otley, A. Prokofjevs, C. Pezzato, M. Owczarek, S. J. Lee, J. W. Choi, J. F. Stoddart, *Nat. Energy* **2018**, *4*, 51–59.

[8] a) H. Wang, Y. Bai, S. Chen, X. Luo, C. Wu, F. Wu, J. Lu, K. Amine, *ACS Appl. Mater. Interfaces* **2015**, *7*, 80–84; b) S. Gu, H. Wang, C. Wu, Y. Bai, H. Li, F. Wu, *Energy Storage Mater.* **2017**, *6*, 9–17; c) J. R. González, F. Nacimiento, M. Cabello, R. Alcántara, P. Lavela, J. L. Tirado, *RSC Adv.* **2016**, *6*, 62157–62164; d) M. Tian, R. Li, C. Liu, D. Long, G. Cao, *ACS Appl. Mater. Interfaces* **2019**, *11*, 15573–15580.

[9] S. Choudhury, Z. Tu, A. Nijamudheen, M. J. Zachman, S. Stalin, Y. Deng, Q. Zhao, D. Vu, L. F. Kourkoutis, J. L. Mendoza-Cortes, L. A. Archer, *Nat. Commun.* **2019**, *10*, 3091.

[10] a) J. Yang, T. Lan, J. Liu, Y. Song, M. Wei, *Electrochim. Acta* **2013**, *105*, 489–495; b) A. Chippindale, P. Dickens, *Solid State Ionics* **1987**, *23*, 183–188.

[11] a) C. V. Ramana, R. J. Smith, O. M. Hussain, M. Massot, C. M. Julien, *Surf. Interface Anal.* **2005**, *37*, 406–411; b) R. Baddour-Hadjean, J. P. Pereira-Ramos, C. Navone, M. Smirnov, *Chem. Mater.* **2008**, *20*, 1916–1923; c) H. Yu, Y. Wu, X. Li, H. Huang, Y. Shi, L. Zhou, *Symposium on Photonics and Optoelectronics (SOPO)* **2011**, 1–3.

[12] Y.-S. Kim, K. D. Harris, B. Limoges, V. Balland, *Chem. Sci.* **2019**, *10*, 8752–8763.

[13] a) M. Demeter, M. Neumann, W. Reichelt, *Surf. Sci.* **2000**, *454*, 41–44; b) G. Silversmit, D. Depla, H. Poelman, G. B. Marin, R. De Gryse, *J. Electron Spectrosc. Relat. Phenom.* **2004**, *135*, 167–175.

[14] A. M. Engstrom, *ProQuest LLC* **2013**, P40.

[15] a) L. Liu, L. Miao, L. Li, F. Li, Y. Lu, Z. Shang, J. Chen, *J. Phys. Chem. Lett.* **2018**, *9*, 3573–3579; b) J. S. Murray, P. Politzer, *Wiley Interdiscip. Rev.: Comput. Mol. Sci.* **2011**, *1*, 153–163.

Manuscript received: October 2, 2019
Revised manuscript received: November 6, 2019
Accepted manuscript online: November 12, 2019
Version of record online: January 3, 2020

© 2019 Wiley-VCH Verlag GmbH & Co. KGaA, Weinheim